The stability of ideal magnetohydrodynamic ballooning modes in plasmas with internal transport barriers

J. W. Connor and R. J. Hastie
Euratom/UKAEA Fusion Association, Culham Science Centre, Abingdon, Oxfordshire, OX14 3DB, United Kingdom

(Received 14 November 2003; accepted 23 January 2004; published online 31 March 2004)

The stability and spatial structures of short wavelength ideal magnetohydrodynamic ballooning modes (i.e., those modes with moderate to large values of the toroidal mode number, n) that can exist in regions of zero or small magnetic shear are investigated. This is a situation relevant to discharges with internal transport barriers (ITBs). The generic properties of such instabilities are discussed by considering the $s-\alpha$ equilibrium. In regions of low s the ballooning formalism fails for large but finite, values of n. In this limit a complementary approach is developed, based on solving the recurrence relation describing the toroidal coupling of radially localized ''modelets'' on adjacent mode rational surfaces. This technique extends the stability analysis to lower s and finite n, capturing effects arising from the discreteness of mode rational surfaces. Consideration of equilibrium trajectories in the $s-\alpha$ stability diagram corresponding to profiles of ITB discharges allows one to determine the global stability of such discharges to these modes. It is shown that the stability of ITBs can be parameterized in terms of $\alpha_{\max}$, the value of the peak α, and the steepness of the barrier pressure profile relative to the shape of the q profile. Inclusion of the stabilizing effects of favorable average curvature at finite aspect ratio, ϵ, leads to stable high-pressure ITB configurations. The stabilizing influence of low-order rational values of $q_{\min}$ also emerges from the theory. The influences of the bootstrap current and plasma flow shear at ITBs are briefly discussed. [DOI: 10.1063/1.1683474]

I. INTRODUCTION

Internal transport barriers (ITBs) in tokamaks[1–6] are associated with low values of the magnetic shear, $s=(r/q)dq/dr$, where $q(r)$ is the radial profile of the safety factor, and by definition necessarily involve a localized steepening of the pressure profile. Thus their stability to short wavelength (i.e., $n\gg 1$, where n is the toroidal mode number) ideal magnetohydrodynamic (MHD) ballooning modes becomes an issue. The generic features of the stability can be understood using the familiar ''$s-\alpha$'' stability diagram [$\alpha=-(2Rq^2/B^2)dp/dr$ is the normalized pressure gradient] which is obtained using the ballooning representation.[7] However this is normally considered in terms of solutions of the lowest order (in $1/n$) ballooning equation and does not take account of the implications of the higher order theory for the radial structure of the modes, $A(x)$, where x is a radial coordinate. To determine this structure one must specify equilibrium profiles as functions of x and solve the lowest order equation for its eigenvalue $k(x,\gamma)$, where γ is the growth rate and k the radial wave number of the mode. A Wentzel–Kramers–Brillouin (WKB) phase-integral determines γ and the mode envelope, $A(x)\sim\exp(i\int k(x)dx)$.

At constant s this mode envelope is centred on the maximum of the $\alpha(x)$ profile. To represent the pressure profile near the ITB, which has a ''pedestal'' structure, we take α in the form:

$$\alpha=\alpha_{\max}\,\mathrm{sech}^2(x/L_*), \tag{1}$$

where $\alpha_{\max}$ is the maximum value of α in the ITB and the length L_* is characteristic of the barrier width. This form describes a shallow, or ''weak,'' ITB as $L_*\to\infty$ and a steep and narrow, or ''strong,'' one as $L_*\to 0$. It is important to stress that the global stability of any profile requires every point on it to be stable. Thus if one utilizes the second stability regime of the $s-\alpha$ stability diagram to achieve high values of $\alpha_{\max}$, one must ensure a route in the diagram that ensures the whole profile lies in stable regions.

The low values of s often associated with ITBs have a profound impact on the radial envelope of extended ballooning modes;[8–10] i.e., the envelope width, $\Delta x/r$, narrows as $(L_*/rnqs)^{1/2}\exp(-c/|s|)$, where $\mathrm{Re}\,c>0$. As a consequence, at small values of s, the envelope width approaches the distance, Δ_{mrs}, between mode rational surfaces and the ballooning representation begins to fail; indeed at sufficiently small s the extended ballooning mode is replaced by a set of independent ''modelets'' that are located at each of the rational surfaces. The transition between extended ballooning mode structures and weakly coupled modelets as s becomes smaller, can be investigated by solving a simple recurrence relation satisfied by adjacent modelets, a technique employed earlier for drift waves.[8,10]

Experimentally it appears that ITBs may occur at a minimum in q where one can write

$$q=q_{\min}+q''x^2/2 \tag{2}$$

so that $s=(rq''/q)x$, where x is the radial distance from the minor radius r corresponding to $q_{\min}$ and primes denote radial derivatives. Since $s\propto x\to 0$ near $q_{\min}$, we see that ex-

tended ballooning modes cannot penetrate to $q_{\min}$. The actual location of the ballooning mode is determined by a competition between the variations of both α and s: the steepness of the pressure gradient, or high values of α, will drive this location towards $q_{\min}$, while the zero in s there will act to prevent this. As a result of the exponentially strong effect of the latter as $s \to 0$, the shape of the resulting envelope will be asymmetric, truncated somewhat on the side of $q_{\min}$. For situations where this competition leads to a mode localized at small values of s, the recurrence relation method is more appropriate.

In Sec. II we introduce the $s-\alpha$ model for ideal ballooning modes and present a mild generalization of the ballooning transformation to accommodate the presence of $q_{\min}$. The standard procedure for calculating the radial envelope, and eigenvalue γ, from the solutions of the lowest order ballooning equation using the WKB phase integral is outlined. In Sec. III we consider a two-scale calculation that is valid at low s and allows an analytic treatment. However this approximation fails to provide the information needed to calculate the radial envelope: the dependence on $k(x,\gamma)$ is exponentially small and lost in this analysis. A variational approach[9,11] allows one to recover this term. These results enable us to deduce the form of the recurrence relation between modelets that complements the ballooning representation as it begins to fail. Analytic solutions of the WKB and recurrence relation approaches are discussed in Sec. IV.

Using the ballooning representation and recurrence relation approaches, Sec. V examines the validity at low s of the $s-\alpha$ diagram for finite, but moderate to large, n, obtaining the finite-n modifications arising from the effects of the α profile, characterized by the scale length L_*, which are valid at low s. Within the ballooning formalism the analysis of the radial structure leads to finite-n corrections to the first stability boundary of the $s-\alpha$ diagram, $\alpha_1(s)$. These corrections are favorable, shifting the marginal α to a slightly higher value. However, the radial analysis also predicts that the second stability boundary, $\alpha_2(s)$, is generally spurious, and that no stable ''global'' equilibrium with $\alpha_{\max} > \alpha_2$ can be found. In contrast, analysis of the radial structure using the recurrence method reveals that, for a given value of n, some second stable regions do survive at low shear; i.e., globally stable equilibria with $\alpha_{\max} > \alpha_2$ do exist. This is an additional finite-n effect associated with the discreteness of mode rational surfaces. It is not captured by the ballooning representation, but is present in the recurrence approach. In a real tokamak these stable regions may not be robust to variations in $q_{\min}$, but could be of value in interpreting MHD code results. We also explore the mode structures emerging from the recurrence method.

As mentioned above, in order to explore the global stability of an equilibrium with an ITB in this model one needs to consider the trajectories in the stability diagram corresponding to the α and s of an ITB discharge. Section VI explores the competition between the low values of s near $q_{\min}$ and the variation of the pressure gradient near the ITB in determining the mode location, structure and stability. Of more practical interest for ITBs in tokamaks, it is shown in Sec. VII that including the stabilizing effects of favorable average curvature (i.e., when $q_{\min} > 1$) (Ref. 12) allows one to identify the conditions for global stability within this simple equilibrium model. While one might naively obtain similar results from the lowest order ballooning theory, the higher order theory has completely failed in this situation and the recurrence relation approach is essential to a consistent theory. A briefer treatment of this section has been published earlier.[13] Section VIII studies the results of the effect of a self-consistent treatment of the bootstrap current on the magnetic shear near an ITB.

Finally effects arising from the presence of a sheared plasma flow, which is often associated with an ITB, are briefly explored in Sec. IX. Section X provides a discussion and draws conclusions.

II. THE $s-\alpha$ EQUATION AND BALLOONING REPRESENTATION

In this section we consider the high-n, ideal MHD ballooning equation for the $s-\alpha$ equilibrium[7] and demonstrate the methods described in Sec. III for determining the mode structure. In terms of a radial coordinate x and a poloidal angle θ this equation takes the form of an equation for the perturbed radial plasma displacement $\Phi(x,\theta,\varphi,t) \propto \exp(in\varphi + \gamma t)\Phi(x,\theta)$, where γ is the growth rate

$$\left(\frac{\partial}{\partial\theta} - inq(x)\right)\left(1 + \left[\frac{ir}{nq}\frac{\partial}{\partial x} + \alpha\sin\theta\right]^2\right)\left(\frac{\partial}{\partial\theta} - inq(x)\right) + \alpha\left\{\cos\theta + \left[\frac{ir}{nq}\frac{\partial}{\partial x} + \alpha\sin\theta\right]\sin\theta\right\}\Phi = \hat{\gamma}^2\Phi. \tag{3}$$

Here $\alpha(x/L_*)$ is given by a form such as (1). We have introduced an eigenvalue $\hat{\gamma}^2$ in Eq. (3) that merely labels stability; this is sufficient for our main purpose of establishing stability boundaries. A more physical interpretation that properly describes the actual growth rate, γ, is given in Appendix A and introduced into our final dispersion relation. When later we examine the global stability of q profiles with a minimum, we shall generalize this equation to include the formally small, in inverse aspect ratio, terms associated with a stabilizing favorable curvature, i.e., the Mercier term.[12]

One approach to solving this equation is to Fourier decompose $\Phi(x,\theta)$ in terms of poloidal harmonics:

$$\Phi(x,\theta) = \sum_m c_m \exp(-im\theta)u_m(x), \tag{4}$$

where $u_m(x)$ is normalized such that its square-integral is unity, but the stability problem remains two-dimensional in x and θ.

However, when the magnetic shear is constant and other equilibrium variations are slow on the scale of the separation of rational surfaces, Δ_{mrs}, one can reduce this two-dimensional problem to two consecutive one-dimensional problems by using the ballooning transformation[7,14,15]

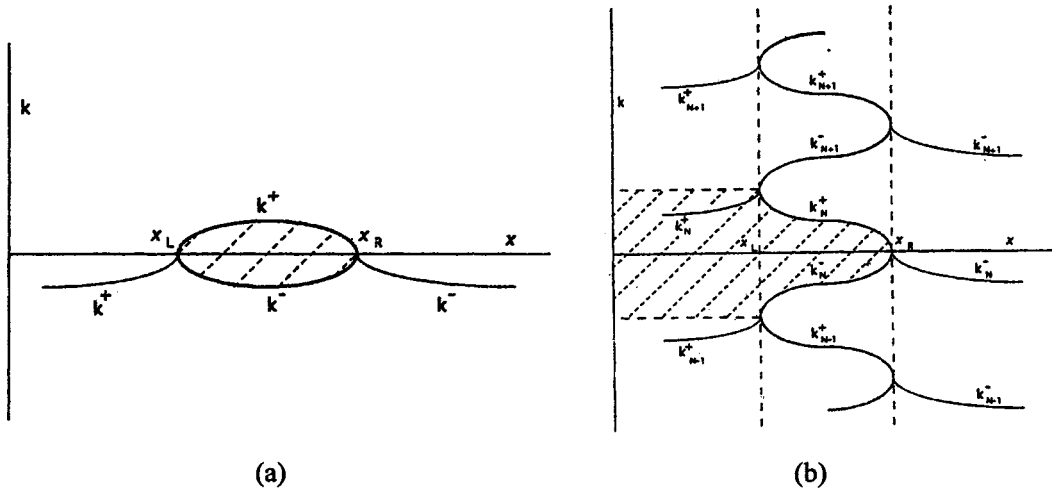

FIG. 1. WKB diagram for the case of (a) standard left and right turning points $x_{L,R}$ given by $k(x_{L,R})=0$ and (b) the multiple branches associated with $\cos k(x)$, in particular showing the principal branches k^+ and k^- and the corresponding turning points given by $\cos k(x_{L,R})=\pm 1$ (Ref. 17). The phase-integral is taken over the shaded area in $k-x$ space in each case.

$$\Phi(x,\theta,\varphi)=\sum_m \exp(-im\theta) \times \int_{-\infty}^{\infty} d\eta \exp(im\eta)\xi(x,\eta,\varphi) \tag{5}$$

in which η is defined on the range $-\infty<\eta<\infty$. One is then permitted to introduce the nonperiodic eikonal form

$$\xi(x,\eta,\varphi) = \exp\left\{ in\left[\varphi - q_0\eta - q' x\eta + q'\int k(x)dx \right]\right\}\zeta(\eta,k) \tag{6}$$

in which $k(x)$, the radial wave number, describes the radial amplitude variation.

The high-n ideal MHD eigenvalue equation for the $s-\alpha$ equilibrium in ballooning space follows from applying the ballooning representation (6) to Eq. (3). The result is the familiar form[7]

$$\frac{d}{d\eta}(1+[s(\eta-k)-\alpha\sin\eta]^2)\frac{d}{d\eta}\zeta + \alpha\{\cos\eta[s(\eta-k)-\alpha\sin\eta]\sin\eta\}\zeta=\hat{\gamma}^2\zeta \tag{7}$$

which determines $\zeta(\eta,k)$ and a local eigenvalue $k(x,\hat{\gamma})$.

If there are WKB turning points, i.e., where $k=0$, so that $k(x)$ defines a closed loop in the $k-x$ plane (with upper and lower branches labeled by k^+ and k^-, respectively), one obtains the usual WKB phase-integral condition[15]

$$nq'\int_{x_L}^{x_R}(k^+-k^-)dx=2\pi\left(\ell+\frac{1}{2}\right), \tag{8}$$

where ℓ is an integer and x_L and x_R are the left- and right-hand turning points: $k(x_{L,R})=0$. The integral (8) is over the shaded area in Fig. 1(a). If we suppose a simple model for k: $k^2=\sigma^2[(\Delta x/L)^2-(x/L)^2]$ so that Δx corresponds to the mode width, then one can estimate $\Delta x\propto(L/\sigma nq')^{1/2}$ from Eq. (8). We shall see later that $\sigma\sim\exp(1/|s|)$.

Alternatively, the trajectories in the $k-x$ plane may be periodic in k and WKB solutions will couple an infinity of branches of $k(x)$ [see Fig. 1(b)]. A treatment of such a problem for constant magnetic shear and linear plasma profiles, i.e., $\propto x/L$, has been given previously,[9,16,17] resulting in the eigenvalue condition

$$nq'\left[\int_{x_L}^{x_R}(k^+-k^-)dx+\pi x_L\right]=2\pi\ell, \tag{9}$$

where now $x_{L,R}$ are the left- and right-hand turning points determined by $\cos k(x_{L,R})=\pm 1$, k^+ and k^- are the two principal branches of k in Fig. 1(b) and ℓ is again an integer. The left-hand side, an integral over x, can be recognized as the shaded area in Fig. 1(b); one can readily convert this to a form expressed as an integral over k.[16] In this case one can estimate $\Delta x\propto L$, the radial distance for $\cos k$ to vary between $+1$ and -1, corresponding to a more extended mode.

However, near a minimum, q can be represented by the parabolic form (2) which leads to a linear dependence of shear: $s\propto x$. The high-n mode stability problem appears to be a two-dimensional problem, namely in poloidal angle θ and radius x. However, as in conventional ballooning theory, it can again be reduced to a succession of two one-dimensional problems by introducing the eikonal representation for the perturbation; but it takes a slightly different form to account for the x variation of s:

$$\xi(x,\eta,\varphi) = \exp\left\{ in\left[\varphi-\eta(q_{\min}+q''x^2/2)+q''\int^x k(x)xdx\right]\right\} \times\zeta(\eta,k). \tag{10}$$

This leads to the replacements:

$$k_\parallel=-(i/Rq)\partial/\partial\eta,\quad k_x=-nq''x(\eta-k), \quad k_\eta=-nq/r. \tag{11}$$

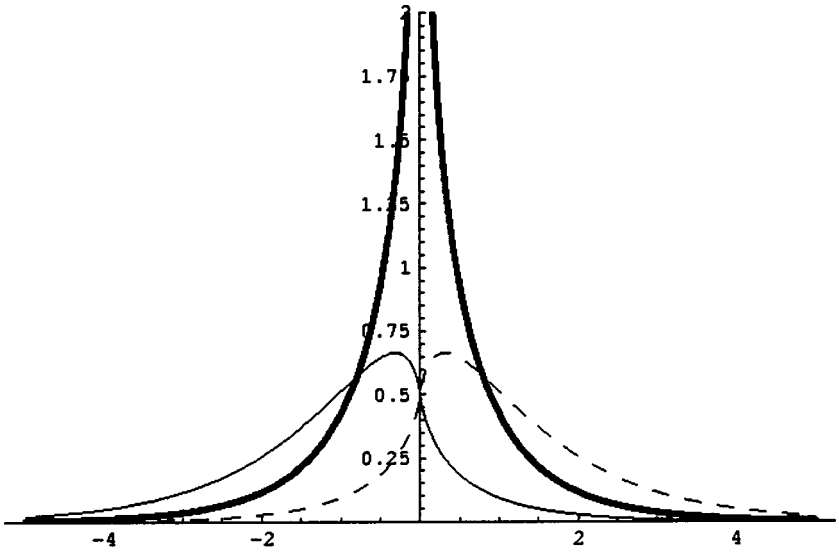

FIG. 2. The $m=0$ (heavy solid line), $m=+1$ (dashed line) and $m=-1$ (solid) harmonics of the ideal MHD ballooning mode eigenfunction, $\Phi(x,\theta)$, corresponding to Eq. (17). The abscissa is $t=(nq'x-m)/s$.

As a consequence one recovers the familiar ballooning equation (7) for $\zeta(\eta,k)$ but with the substitution:

$$s\rightarrow rq''x/q\equiv\mu x/r \tag{12}$$

so that there is an additional equilibrium dependence on x in the ballooning equation.

The phase-integral eigenvalue conditions (8) and (9) are also modified: thus in place of these we have, respectively,

$$nq''\int_{x_L}^{x_R}(k^+-k^-)xdx=2\pi(\ell+1/2), \tag{13}$$

$$nq''\left[\int_{x_L}^{x_R}(k^+-k^-)xdx+\pi x_L^2/2\right]=2\pi\ell. \tag{14}$$

The left-hand side integral over x in Eq. (13) can now be recognized as the x-moment over the area of the loop in Fig. 1(a), that in Eq. (14) the same moment over the shaded area in Fig. 1(b); as before one could readily convert these to forms expressed as integrals over k.[16] If the turning points are close and not too near $x=0$, so that they can be approximated by some average value x_0, these conditions reduce to the standard forms with $x_0q''\approx q'(x_0)$.

III. ANALYSIS FOR LOW SHEAR

To apply the analysis discussed in Sec. II, it is helpful, and instructive, to use analytic solutions for the eigenvalues of the lowest order ballooning equation (7). Fortunately such an expression has been derived by Pogutse and Yurchenko[11] using trial functions in a variational form for Eq. (7). The trial function is based on a two-scale solution of Eq. (7) valid for small s. In this approach one introduces a slow dependence of ζ on a scale $u=s(\eta-k)$, the natural scale of the secular terms in Eq. (7) (i.e., there is a "stretching" parameter, s), in addition to the periodic variation on 2π. We briefly sketch the outline of their approach here.

Defining $G=1+[s(\eta-k)-\alpha\sin\eta]^2$ and introducing $V=\zeta G^{1/2}$, we can write Eq. (7) in the "Schrödinger-type" form

$$G\frac{d^2V}{d\eta^2}+V\left\{\frac{1}{4G}\left(\frac{dG}{d\eta}\right)^2-\frac{1}{2}\frac{d^2G}{d\eta^2}+\alpha[\cos\eta+\sin\eta(s(\eta-k)-\alpha\sin\eta)]+\hat{\gamma}^2\right\}=0. \tag{15}$$

After redefining the origin of $\eta\,(\eta\rightarrow\eta-k)$ it is convenient to introduce the two-scale approach, writing $\partial/\partial\eta\rightarrow\partial/\partial\eta+s\partial/\partial u$ and developing a self-consistent expansion, $V=V_0+V_1+\cdots$ in powers of α with the ordering $s\sim\alpha^2$. In leading order $dV_0/d\eta=0$, i.e., $V_0=V_0(u)$, while in first order one obtains

$$V=V_0(u)\left[1+\frac{\alpha\cos\eta}{1+u^2}\right]. \tag{16}$$

Eventually one finds an equation for $V_0(u)$ in $O(\alpha^4)$;[11,18] however for our purposes one can follow Ref. 11 and adopt a variational approach, using a trial function for V given by Eq. (16) with $V_0=1$ chosen for simplicity.

It is instructive to calculate the $\Phi(x)$ that results from this trial function. Inverting the ballooning transform for ζ from V (after accounting for the factor G), by the necessary Fourier transform, one finds

$$\Phi(x,\theta)=e^{-im\theta}K_0(|t|)+(\alpha/2)\Sigma_{\pm}e^{-i(m\pm1)\theta}[|t|K_1(|t|)\pm tK_0(|t|)], \tag{17}$$

where $t=(nq'x-m)/s$ and K_0 and K_1 are modified Bessel functions. Figure 2 shows the radial shape of the Fourier harmonics in Eq. (17). An important point is that these localized, isolated modes, located at each of the rational surfaces are not pure Fourier modes, but "modelets" containing weak sidebands. (If the coupling to sidebands were stronger and

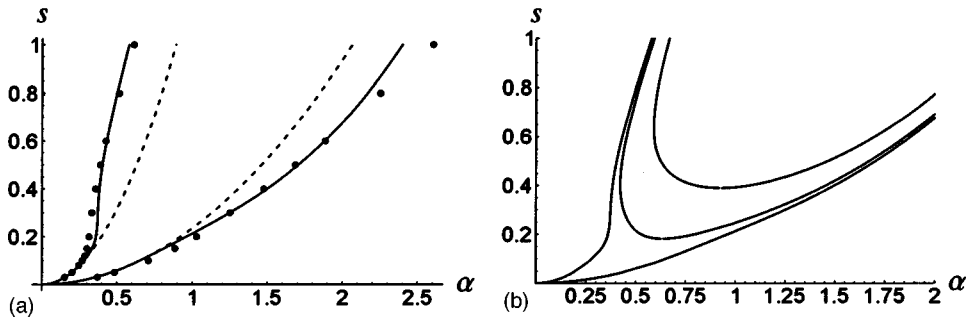

FIG. 3. (a) The $s-\alpha$, infinite-n, marginal stability boundaries at low shear, using the variational method Eq. (19). Dashed curves from two-scale power series expansion with $s\sim\alpha^2\ll 1$; solid curves include $\exp(-1/|s|)$ terms. Discrete points are from numerical solutions of the full $s-\alpha$ equation. (b) Variational stability boundaries in the presence of favorable average curvature: $q=3/2$ and $\epsilon=0$, 0.05, and 0.3, where the higher values of ϵ are further from the origin.

the modelet had significant harmonic content, the localization would continue to be primarily controlled by the smallness of s.) The choice of V_0 in Eq. (16) is satisfactory for marginal stability, $\gamma=0$, but does not capture the correct convergence of V_0 at large t due to inertial effects; as a result it leads to the logarithmic singularities at $x=0$ in $K_{0,1}$, evident in Fig. 2. A modification to V_0 for $\gamma>0$ which removes this effect is discussed in Appendix A.

Equation (15) can be derived from the variational quantity

$$H=\int_{-\infty}^{\infty}\left[\left(\frac{dV}{d\eta}\right)^2-\frac{1}{G}\left\{\frac{1}{4G}\left(\frac{dG}{d\eta}\right)^2-\frac{1}{2}\frac{d^2G}{d\eta^2}+\alpha[\cos\eta+\sin\eta(s(\eta-k)-\alpha\sin\eta)]+\hat{\gamma}^2\right\}V^2\right]d\eta. \tag{18}$$

First we expand $G^{-1}=(1+u^2)^{-1}\Sigma_n\alpha^n(G^{-1})_n$, retaining terms up to $n=3$, and insert this form into H, collecting the coefficients of the different harmonics in η. The contributions to H from terms harmonic in η can be readily evaluated by contour integration, expressing them in terms of the residues at the poles of $(1+u^2)^{-1}$, i.e., where $\eta-k=\pm i/s$. Since a term such as $\cos p\eta$ produces a contribution that is exponentially smaller, i.e., $\propto\exp(-p/|s|)$, one need only retain terms in $\cos\eta$ and $\sin\eta$ in the integrand of H in Eq. (18). Thus, on substituting the trial function V as given by Eq. (16) in the variational equation (18), $H=0$, we finally obtain an eigenvalue equation

$$\hat{\gamma}^2+s^2/2-(5\alpha/4)\exp(-1/|s|)\cos k-3s\alpha^2/4+(19/128)\alpha^4=0, \tag{19}$$

where we have followed Ref. 11 in only retaining the contributions linear in α in the $\cos k$ term. It is convenient for later to introduce $\gamma_0^2=-(s^2/2-3s\alpha^2/4+(19/128)\alpha^4)$, describing the growth rate in the absence of the $\cos k$ term. In Appendix A we show that the "fictitious" eigenvalue $\hat{\gamma}^2$ corresponds to γs, where γ is the actual linear growth rate normalized to the Alfvén frequency. Appendix B presents a more accurate treatment of the variational approach to this dispersion relation that indicates that Eq. (19) is indeed a reasonable approximation. Equation (19) can be solved for $k(x,\hat{\gamma})$, where the x-dependence originates from the profile of $\alpha(x/L_*)$ if s is constant, or from $s=\mu x/r$ and α if there is a minimum in q.

Equation (19) is close to the form derived in Ref. 11, but differs slightly in the numerical coefficients. However it captures the key features of the full $s-\alpha$ marginal stability diagram to approximately 10% accuracy (indeed slightly more accurately than Ref. 11), as shown in Fig. 3(a). Thus for small s and α it obtains the first and second stability boundaries as $\alpha^2/s=0.77$ and 4.56 (i.e., to less than 4% accuracy for α on the first stability boundary) and, furthermore, the term in $\exp(-1/|s|)$ arising from the variational principle ensures it is equally accurate at finite values of s and α.

It is worth emphasizing again that it is only through the variational approach that one can extract the nonanalytic dependence on s in the exponential function in Eq. (19); this term, which represents the weakening of toroidal coupling at low magnetic shear, was lost in the simple two-scale solution $V_0(u)$ of Eq. (16). The key element supplied by the variational treatment of Ref. 11 is the reappearance, in the zero order ballooning solution, of the true eigenvalue $k(x,\hat{\gamma})$. As a result a calculation of radial model structure becomes possible.

The asymptotic analysis in powers of $s^{1/2}$ for low shear has been performed previously on the $s-\alpha$ equilibrium model[18] and also in an expansion of a general equilibrium around the magnetic axis.[19–22] Slightly different equations for $V_0(u)$ emerge in these two problems, but in all cases no dependence on k is found since the $O(\exp(-1/|s|))$ coefficient of k obtained by the variational method is not captured by the asymptotic expansion method.

The $s-\alpha$ equilibrium neglects terms in the inverse aspect ratio, ϵ. However including these introduces the stabilizing (if $q_{\min}>1$) effect of favorable average curvature, or the "Mercier" term, d_M, where[11]

$$d_M=\epsilon\alpha(1-q^{-2}). \tag{20}$$

This appears as an additional term on the left-hand side of Eq. (7), added to the term in α. This can be readily followed through the analysis and modifies Eqs. (15), (18), and (19), leading to the substitution

$$\gamma_0^2\rightarrow\gamma_0^2-d_M. \tag{21}$$

The effect of d_M on the $s-\alpha$ diagram is shown in Fig. 3(b). We will return to the effect of d_M when we discuss ITBs with a minimum in q in Sec. VII.

IV. SOME ANALYTIC RESULTS

If for the moment we suppose that the shear, s, is constant and the pressure profile variation leads to a quadratic dependence of γ on x/L, where x is measured from the most unstable position and L represents this equilibrium variation, then neglecting d_M for simplicity, we can write Eq. (19) in the form

$$\hat{\gamma}^2-\gamma_0^2-(x/L)^2-2\lambda\cos k=0, \tag{22}$$

where we have defined $\gamma_0^2=-(s^2/2-3s\alpha^2/4+(19/128)\alpha^4)$, $L^{-2}=d^2\gamma^2/dx^2$ and $\lambda=(5\alpha/8)\exp(-1/|s|)$. If we expand $\cos k\approx 1-k^2/2$ for small k and introduce this into the WKB condition (8), we obtain an eigenvalue condition

$$\hat{\gamma}^2=\gamma_0^2+2\lambda-(2\ell+1)(2\lambda)^{1/2}/(nq'L) \tag{23}$$

and mode width

$$\Delta x/r=[(2\ell+1)(2\lambda)^{1/2}L/(nq')]^{1/2}$$
$$\sim\exp(-1/4|s|)(L/rsnq)^{1/2}. \tag{24}$$

Clearly this becomes very narrow as $s\to 0$ so that the validity condition for the ballooning representation [namely that Δx, the width of the mode envelope $A(x)$, satisfies $\Delta x \gg \Delta_{\mathrm{mrs}}=r/(snq)$, the separation of mode rational surfaces], is then in question for physically reasonable, finite values of n. In the case of the more extended modes that exist for a linear profile of γ_0^2, i.e., away from the maximum in γ_0^2, the mode width is given by the range of x needed for $\cos k$ to range between ± 1. One deduces

$$\Delta x=4\lambda L_1\sim\exp(-1/|s|)L_1, \tag{25}$$

where $L_1^{-1}=d\gamma_0^2/dx$. As shown in Appendix C, Eq. (C5), the eigenvalue takes the form

$$\hat{\gamma}^2=\gamma_0^2+(x_0/L_1), \tag{26}$$

where x_0 is the arbitrary center of the mode. It is interesting that this "extended" mode (25) can become narrower than the "localized" mode (24) as $s\to 0$. Similarly we expect that the radial mode structure will be strongly affected by the presence of a stationary point in $q(r)$ [i.e., at $x=0$, when $s=(rq''/q)x\equiv\mu x/r$].

When $\Delta x\sim\Delta_{\mathrm{mrs}}$ one can consider a complementary approach based on a recurrence relation between the amplitudes of modelets on each rational surface, i.e., the c_m in Eq. (4).[8,10] This relation could be determined by substituting the form (17) in Eq. (4) and integrating over x and θ. In general this will couple the different c_m due to toroidal effects, the strength of the coupling also involving overlap integrals between the corresponding $u_m(x)$. As we have seen in Eq. (17) and Fig. 2, at low s the $u_m(x)$ are localized near $x=m/(nqs)$ so that only adjacent values of m will couple. Furthermore, any dependence on x can be replaced by one on the corresponding value of $m/(nqs)$.

However one can determine the resulting structure of the recurrence relation from the dispersion relation directly from Eq. (19) as follows. In the ballooning limit the c_m are slowly varying; indeed, as equilibrium variations approach zero they are constant up to a phase factor, i.e., one can set $c_m=\exp(ikm)$. If the resulting dispersion relation is to lead to Eq. (19), then one can see that the recurrence relation must have the "three-term," or "tridiagonal" form

$$[\hat{\gamma}^2-\gamma_0^2(s,\alpha)]c_m-(5\alpha/8)\exp(-1/|s|)[c_{m+1}+c_{m-1}]=0, \tag{27}$$

where $\alpha=\alpha(x/L_*)\to\alpha(m/(nqsL_*)$. The validity of relation (27) depends only on low s; unlike the ballooning representation, this implies that no constraints are placed on the parameter $L_*/\Delta_{\mathrm{mrs}}=nsqL_*/r$.

The brief discussion above was in terms of the coupling between Fourier harmonics on adjacent surfaces. Strictly we have seen that the modelets (17) contain sidebands of order α, but these are still localized at the common surface. So the recurrence relation represents the coupling of these modelets, rather than simple Fourier modes. The contribution of the sidebands is reflected in the $O(\alpha^2)$ and $O(\alpha^4)$ terms in γ_0^2. More generally the modelets might contain stronger harmonic content but because of the low shear they would remain localized and the recurrence relation would continue to involve coupling of the appropriate modelets on adjacent rational surfaces, i.e., remain a three-term recurrence relation.

To discuss the nature of the solutions of the recurrence relation it is convenient to expand γ_0^2 about its maximum in x (or m). Schematically one can then rewrite relation (27) as

$$[\hat{\gamma}^2-\gamma_0^2-\kappa m^2]c_m-\lambda[c_{m+1}+c_{m-1}]=0, \tag{28}$$

where $\kappa=(1/nq')^2d^2\gamma_0^2/dx^2=(r/snqL)^2$. Clearly the solutions depend only on a single parameter: $\nu=\lambda/\kappa$. The solution of such a recurrence relation can be expressed in terms of Mathieu functions,[23] as discussed in Ref. 8. However it is clear that for $\nu\to 0$, it consists of a set of independent c_m, each having an eigenvalue appropriate to $x=m/(nqs)$. For small but finite ν, simple perturbation theory shows that[23]

$$\hat{\gamma}^2=\gamma_0^2-\lambda^2/(2\kappa). \tag{29}$$

On the other hand, when $\nu\gg 1$, the c_m become slowly varying in m and many m are coupled, producing an extended ballooning-like structure. To estimate the width Δm in m, one can consider the discrete c_m to be continuous functions of m, $c(m)$. Equation (28) then becomes a second order differential equation for $c(m)$:

$$\frac{d^2c}{dm^2}+\left(\Gamma-\frac{m^2}{\nu}\right)c=0, \tag{30}$$

where the eigenvalue $\Gamma=(\hat{\gamma}^2-\gamma_0^2)/\lambda-2$. It follows that $\Delta m\sim\nu^{1/4}\gg 1$ and the lowest eigenvalue is given by $\Gamma=\nu^{-1/2}$, corresponding to

$$\hat{\gamma}^2=\gamma_0^2+2\lambda-(\lambda\kappa)^{1/2} \tag{31}$$

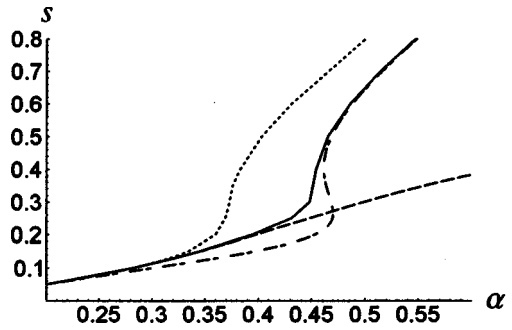

FIG. 4. Finite-n corrections to infinite-n stability, using the recursion method ($n=15$, $q=5/3$, $L_*/r=0.2$, and $\Delta q=0$). Solid curve from exact solution of Eq. (27); dashed curve is the analytic result (29) for $nq\exp(-1/2|s|)\ll 1$; chain curve is the analytic approximation (31) for $nq\exp(-1/2|s|)\gg 1$; dotted curve is the infinite-n boundary.

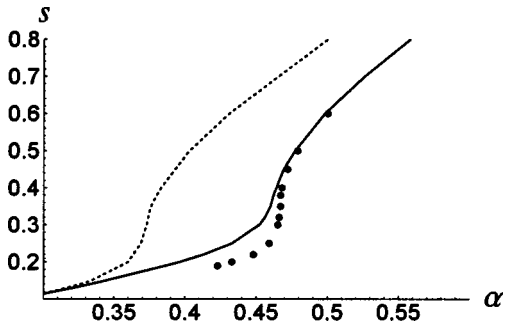

FIG. 5. Comparison of the $s-\alpha$ stability boundary at $n=15$, $q=5/3$, $L_*/r=0.2$, and $\Delta q=0$, from solution of the full recursion equations (solid line) and WKB ballooning formalism (solid points). The WKB approximation fails for low s where the solid points terminate. The infinite-n boundary is shown as a dashed curve.

which is equivalent to the result (23). Equations (23) or (31) reveal a stabilizing shift of the first stability boundary, with magnitude

$$\delta\alpha_1 \sim (\lambda\kappa)^{1/2} \sim (1/nqs)\exp(-1/2|s|). \tag{32}$$

These are the familiar $1/n$ stabilizing corrections to the infinite-n ballooning theory. There is no similar prediction for the second stability boundary. An equilibrium in which $\alpha_{\max}>\alpha_2$ will, of necessity, contain α values which will correspond to the maximum possible growth rate, and a finite-n ballooning mode will appear at the corresponding part of the pressure profile. Thus no ''second stable'' equilibria can exist.

For arbitrary ν one can write $\hat{\gamma}^2=\gamma_0^2+\kappa a_0(\nu)$, where a_0 is the lowest eigenvalue of the Mathieu equation, shown in Fig. 20.1 of Ref. 23; in fact result (31) remains reasonably accurate down to $\nu\sim 5$. The marginally stable $s-\alpha$ curve for $n=15$ predicted by the recurrence relation approach is plotted in Fig. 4 and compared with the strongly coupled result (31) and the weakly coupled result (29). The $n\to\infty$ result is shown for comparison (dotted curve), indicating the stabilizing effects of finite-n. We note that at finite-n one must specify the position of the nearest mode rational surfaces $m_0=nq(x)$ relative to $\alpha_{\max}$. This is characterized by $\Delta q=m_0-nq$; Fig. 4 assumes $\Delta q=0$.

One can also consider the case where γ_0^2 is a linear function of x, which led to the ''extended'' ballooning modes. Equation (28) is replaced by

$$(\hat{\gamma}^2-\gamma_0^2-\kappa_1 m)c_m-\lambda(c_{m+1}+c_{m-1})=0, \tag{33}$$

where $\kappa_1=(1/nq')d\gamma_0^2/dx=(r/snqL_1)$. As shown in Appendix C, one can obtain an analytic solution for $\hat{\gamma}^2$ and the c_m for arbitrary $\nu_1=\lambda/\kappa_1$.[24] We find $c_m=J_{m-p}(2\nu_1)$, corresponding to $\Delta m\sim\nu_1$, where the integer p labels the eigenvalue:

$$\hat{\gamma}^2=\gamma_0^2+p\kappa_1. \tag{34}$$

Thus p specifies where, i.e., $m=p$, along the linear profile the mode is centered. The result (34) corresponds to Eq. (26).

V. STABILITY AT LOW SHEAR

In the previous section we have discussed the impact of low shear on the validity of the ballooning representation used to calculate the $s-\alpha$ stability diagram. Its validity depends on the parameter $\nu\gg 1$, i.e., $s\gg\{2\ln[r/(snqL)]\}^{-1}$ or, alternatively, $n\gg(r/sqL)\exp(1/2|s|)$. In principal one can always choose sufficiently large n to satisfy this, but for realistic values, say $n\sim 50$, this requires $s\gg 0.1$. Even if we assume sufficiently large n, the application of the simple WKB condition (8) has limited validity. Thus if we estimate $k\sim 1/(nq'\Delta x)$ with Δx from Eq. (24), then as $s\to 0$, k is no longer small; indeed once $k\sim 1$ one must retain the full $\cos k$ function to solve for $k(x)$. Then as $k\to\pi$ and $\cos k\to -1$ one loses the WKB potential well and one can only consider the extended modes satisfying Eq. (33). This is found to occur when $s=1/\{2\ln[(2^{1/2}/\pi^2)r/(snqL)]\}$; such a boundary has been confirmed by a full numerical solution of Eq. (7), as shown in Fig. 5. However, as Eq. (25) demonstrates, the widths of the extended modes in this case are comparable with Δ_{mrs} and the ballooning representation is again inappropriate.

It is therefore necessary to use the recurrence relation approach to determine stability and mode structures at low s for realistic n values. It is clear from Eqs. (23) and (31) and Ref. 23 that for the case of a ''quadratic potential,'' κx^2, the stability boundary given by the WKB approach remains valid

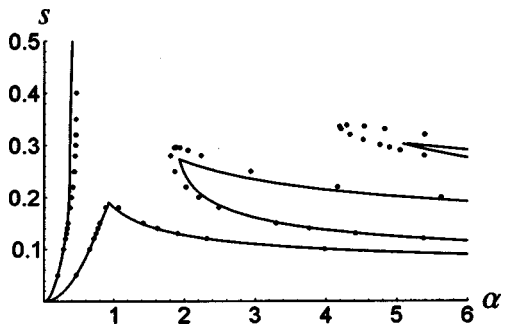

FIG. 6. Second stable bands at finite-n: $n=15$, $q=5/3$, $L_*/r=0.2$, and $\Delta q=0$. Solid points are by solution of the recursion equations; continuous curves are by analytic construction using the infinite-n stability boundaries and the discreteness of the mode rational surfaces.

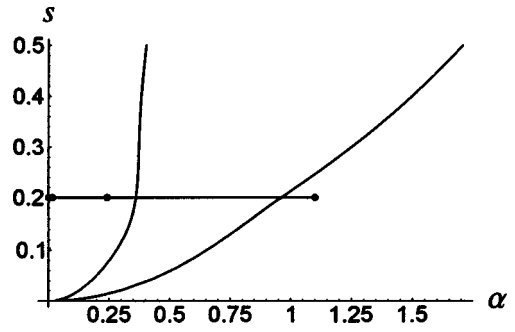

FIG. 7. Location of the discrete mode rational surfaces, x_m, in $s-\alpha$ space for $s=0.2$, x_m given by $\alpha=\alpha_{\max}\,\mathrm{sech}^2(x_m/L_*)$, with $\alpha_{\max}=1.1$, $L_*/r=0.2$, $n=12$, and $q=3/2$. The infinite-n stability boundaries are also shown.

down to $\nu=\lambda/\kappa\sim 5-7$, at which point the corrections to the two-scale growth rate, γ, are negligible. We return to the more complete form (1) for $\alpha(x)$ with $x=m/(nqs)$ and insert it in the recurrence relation (27). Figure 5 also shows a comparison of the solution with the WKB approximation. [Clearly, for sufficiently small values of the argument of $\alpha(x/L_*)$ the result reduces to the quadratic form in Eq. (28) and the analytic solution of Sec. IV.]

Figure 6 shows the resulting impact of finite-n on the $s-\alpha$ stability diagram at low s. As discussed in Secs. III and IV, both the destabilizing effects of ballooning, i.e., coupling between adjacent rational surfaces, and the stabilizing effects of finite-n become exponentially weak at low values of s. Thus the "first" stability boundary, $\alpha_1(s)$, is close to the original $s-\alpha$ curve. As noted earlier, the stabilizing effects are the usual $1/n$ stabilizing corrections to the infinite-n ballooning theory, but there is no corresponding prediction for the second stability boundary. An equilibrium profile with $\alpha_{\max}>\alpha_2(s)$ will necessarily contain α values in the unstable range, $\alpha_2>\alpha>\alpha_1$, thus a finite-n ballooning mode will appear at that part of the profile corresponding to the maximum possible growth rate.

However, because we are using the recurrence approach which is valid at arbitrarily small shear, we find a different finite-n effect and this does predict that a second stability boundary survives at low s, as shown in Fig. 6. This can be understood as follows. At finite values of n the different rational surfaces correspond to discrete differences in α. Then one can have a situation in which $\alpha_{\max}>\alpha_2$ while adjacent rational surfaces correspond to $\alpha<\alpha_1$, so that one can expect the whole profile to be stable. If, for definiteness, we suppose the surface $m=0$ to be at $\alpha_{\max}$, then the $m=\pm 1$ surfaces have $\alpha=\alpha_{\max}\,\mathrm{sech}^2(r/nqL_*s)$. These rational surfaces can be considered to be "beads" lying on a constant s slice through the $s-\alpha$ diagram, as shown in Fig. 7. Thus we have a stable band if $\alpha_{\max}>\alpha_2$ and $\alpha_1>\alpha_{\max}\,\mathrm{sech}^2(r/nqL_*s)$. Similarly, if all three surfaces, $\alpha(m=0,\pm 1)$, lie in the region $\alpha>\alpha_2$ while $\alpha(m=\pm 2)$ satisfy $\alpha<\alpha_1$, a further band exists, and so on. The left-hand tips of the higher bands rapidly migrate rightwards to very large α and need not be considered for reasonable values of $\alpha_{\max}$. These stable bands are shown in Fig. 6 and reflect the structure of the recurrence relation solutions. Of course, as $\alpha_{\max}$ continues to increase one must consider higher and higher bands with values of α lying in the tail of the pressure profile (1) so that adjacent harmonics will have almost the same α; it then becomes impossible to bridge the unstable zone. But because of the rightward migration of the bands this only occurs for extremely large $\alpha_{\max}$. These finite-n results are reminiscent of the stability of low n "infernal" modes that occur at low shear.[25]

This argument supposed that the $\alpha_{\max}$ corresponded exactly to a rational surface; if $m-nq=\Delta q\neq 0$ the situation is more complex. Because of the symmetry of $\alpha(x)$ one need only consider $\Delta q>0$ and since $\Delta q\rightarrow\Delta q+1$ merely corresponds to a relabelling of m_0, it is sufficient to consider $0<\Delta q<1$. Figures 8(a) and 8(b) show representative examples: namely for $\Delta q=1/4$ and $1/2$. The bands are displaced and change in width: for $\Delta q=1/4$ they are narrower and lower, broadening and lifting for $\Delta q=1/2$. Thus as Δq is varied, the bands of $s-\alpha$ stability in the second stable zone distort and migrate in a complex manner. However it is clear that if all values of Δq in $[0,1]$ are admissible, then no second $s-\alpha$ stable region survives. One can see this as follows. Suppose the stable band arises because the first mode rational surface at $\alpha_{\max}$ lies in the second stability region, $\alpha_2<\alpha$, and the next one is below the first stability boundary, $\alpha<\alpha_1$. Then as Δq increases from 0 to 1 at constant s, the position of the first mode rational surface migrates to lower values in α until it reaches the position of the next mode rational surface, i.e., $\alpha<\alpha_1$. Thus it must have passed through the unstable band, $\alpha_1<\alpha<\alpha_2$, on the way. Since, in general, a tokamak can adopt any value of Δq during the evolution of its q profile, particularly at higher n values, this cannot be regarded as a controllable parameter and these

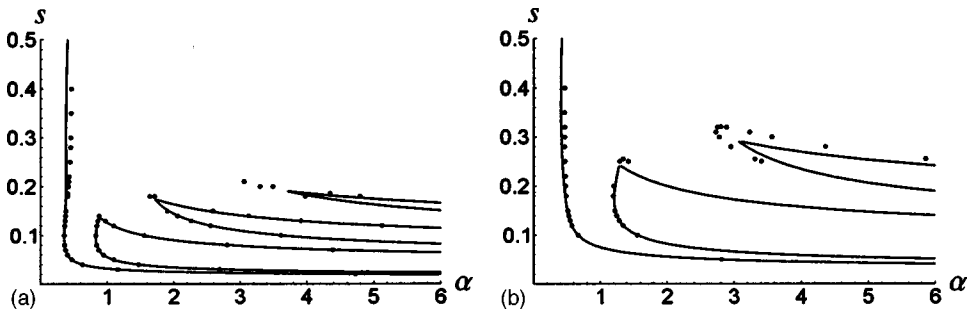

FIG. 8. Second stable bands at $n=15$, $q=5/3$, $L_*/r=0.2$ for (a) $\Delta q=1/4$; (b) $\Delta q=1/2$.

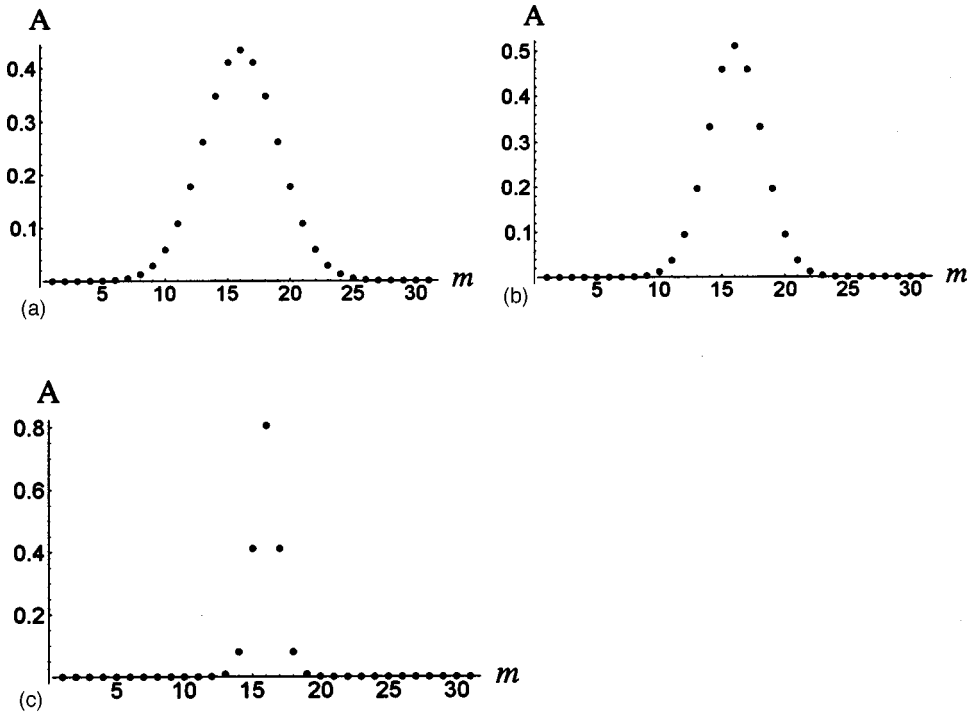

FIG. 9. The amplitudes, $A(m)$, of three typical spectra of poloidal harmonics at marginal stability, showing a progressive narrowing as the shear is reduced. (a) $s=1$; (b) $s=0.5$; and (c) $s=0.2$ ($n=50$, $q=2$, $\mu=1$, $L_*/r=0.2$, and $\Delta q=0$).

bands have little practical significance. However these insights on stability may be of value in interpreting the output of MHD stability codes. We will return to this topic when we discuss ITBs at a minimum in q, where these finite-n effects from $\Delta q=m_0-nq_{\min}$ may play an important role.

It is also interesting to examine the variation of the spectrum in m of the eigenmodes as s decreases. As shown in Fig. 9, this spectrum narrows as s decreases. Indeed, in the limit $s\to 0$ only isolated modelets remain.

VI. STABILITY OF AN ITB AT A MINIMUM IN THE SAFETY FACTOR

The form (1) can also be used to examine the role of a radial profile in α in the presence of $q_{\min}$ when s is given by Eq. (12), a situation relevant to ITBs. Since we are interested in regions of x corresponding to low s, we shall adopt the recurrence relation approach alone as we have seen above that it remains valid for all n. Since the rational surfaces correspond to $m=nq(x)$, when $\Delta q=m_0-nq_{\min}=0$ we can replace x in Eqs. (1) and (12) in terms of m using

$$x_m=\pm(2m/nq'')^{1/2} \tag{35}$$

so the rational surfaces appear in pairs for given $m>0$, one on each side of $q_{\min}$. The $s-\alpha$ model predicts stability for $s<0$, so we need only consider surfaces with $x>0$. Because of the localization of the modelets, coupling to those with $x<0$ through nonresonant poloidal harmonics,[26] i.e., those with $m<nq_{\min}$ so that they have no mode rational surface in the plasma, is extremely weak. It should be noted the harmonic content of each modelet also involves coupling to nonresonant modes, but ones located at the same mode rational surface.

We introduce expressions (1), (12), and (35) into the recurrence relation (27). The dependence of s on m introduces a strong m-dependence into the coupling term. For simplicity, we neglect the slight asymmetry in the coupling of modelets centred at x_m to those at $x_{m\pm1}$ due to the radial variation of the shear between x_{m+1} and x_{m-1}; for smaller m, where it becomes more significant, the coupling is weak anyway. We can identify three parameters: $\alpha_{\max}$, $r^2/(\mu L_*^2)$, and $\mu/(nq)$. The second parameter originates from the radial variation of α at fixed nq and, likewise, the third results from that of s. While the last of these parameters clearly measures the effect of finite-n, the first two define a trajectory in the $s-\alpha$ stability diagram corresponding to the radial profiles of s and α through the ITB. As we move from $q_{\min}$, where $s=0$ and $\alpha=\alpha_{\max}$, the direction of this trajectory is controlled by the parameter $r^2(\mu L_*^2)$. Consequently, in the absence of finite-n effects, one moves from the second stability region, through an unstable band of α before emerging into the first stability region.

As in the case of constant s, it is possible to find stable bands for $\alpha_{\max}>\alpha_2(s)$ at finite-n, due to the discrete spacing of mode rational surfaces. This is displayed in Fig. 10 where the trajectory of α given by Eq. (1) when $\alpha_{\max}$ coincides with $q_{\min}$, is shown in the $s-\alpha$ stability diagram. The discrete mode rational surfaces in this figure correspond to the choice $n=12$, $q_{\min}=3/2$. However, as pointed out in Sec. V, although a particular mode number, n, corresponds to one

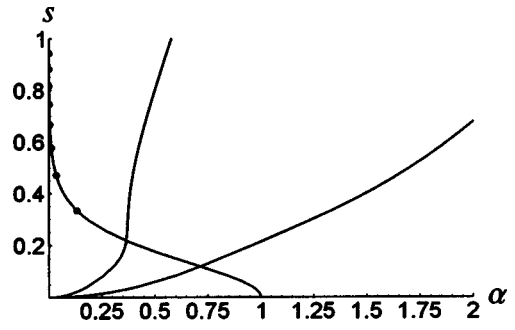

FIG. 10. The $s-\alpha$ stability diagram from the recurrence relation and the equilibrium trajectory and location of the mode rational surfaces in $s-\alpha$ space near a minimum in q ($n=12$, $q=3/2$, $\mu=1$, $L_*/r=0.2$, $\alpha_{\max}=1$, $\Delta q=0$).

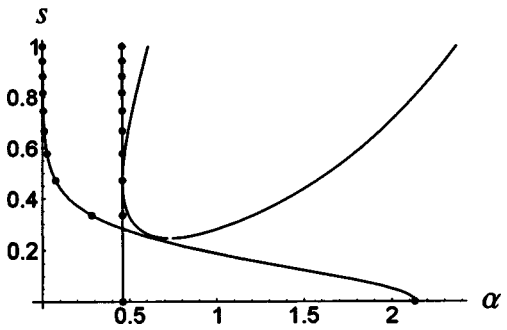

FIG. 12. Trajectories and locations of mode rational surfaces (dots) in $s-\alpha$ space for two marginally stable profiles: $\alpha_{\max}=2.13$, $L_*/r=0.2$ and $\alpha_{\max}=0.46$, $L_*/r=10$ ($n=12$, $q=3/2$, $\mu=1$, $\Delta q=0$). The stability boundary modified by favorable average curvature, d_M, is shown for $\epsilon=0.1$.

particular value of $\Delta q=m_0-nq_{\min}$, other choices of n (and m_0) produce many different values of Δq in the range $0<\Delta q<1$. If Δq is varied continuously from zero to unity the mode rational surface at $q_{\min}$ moves continuously along the trajectory in $s-\alpha$ space, and must inevitably pass through the unstable band $[\alpha_1,\alpha_2]$. This suggests that in endeavoring to interpret data from real discharges, we should regard all values of Δq as available. In this case, finding a globally stable equilibrium with an ITB at $q_{\min}$ becomes impossible. However, it is worth remarking that when the minimum value of q coincides with a low-order rational, the possible values of Δq are greatly restricted. In the extreme case where $q_{\min}$ is an integer, only one value of Δq (i.e., $\Delta q=0$) is possible. In this case the discreteness of the mode rational surfaces at finite-n may play an important role in permitting higher values of $\alpha_{\max}$.

The corresponding spectra in m of the eigenmodes, see Fig. 11 for an example, are offset from $m=0$, i.e., $q_{\min}$, and are somewhat asymmetric, in contrast to the results in Fig. 9. This asymmetry is because the coupling between adjacent m vanishes exponentially, i.e., as $\exp(-1/|s|)$ on the small s side near $q_{\min}$. Larger values of $r^2/(\mu L_*^2)$, corresponding to steeper pressure profiles in the ITB, push the peak of the spectrum nearer $m=0$. Thus, the resulting spectrum is the outcome of a competition between the presence of $q_{\min}$, which excludes the mode from $m=0$, and the steepness of the pressure profile at the ITB which drives the mode towards $m=0$. While the latter can have an effect, it can never win because of the exponentially weak coupling near $q_{\min}$. However, since the spectrum peaks where γ_0^2 is a maximum, its shape is largely dominated by the α profile and the asymmetry is relatively weak.

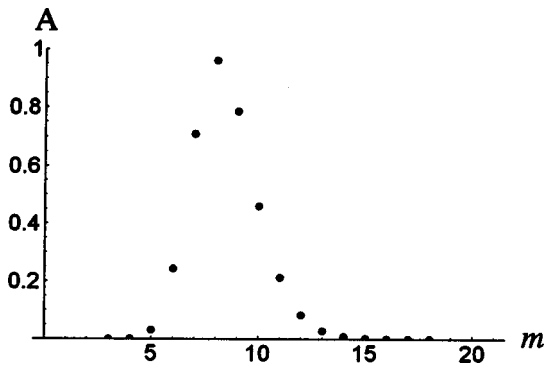

FIG. 11. The amplitudes $A(m)$ of the m-spectrum for $n=100$ ($q=3$, $\mu=1$, $L_*/r=0.3$, $\Delta q=0$, $\alpha_{\max}=1$).

VII. EFFECT OF FAVORABLE AVERAGE CURVATURE

We have seen that for sufficiently large n the $s-\alpha$ equilibrium is inevitably unstable for ITB profiles at some radial point. However, the picture is changed by the inclusion in the model of stabilizing favorable curvature when $q_{\min}>1$, i.e., the Mercier term, d_M, in Eq. (21) that is formally small in the inverse aspect ratio, ϵ. This is because this term has the effect of preventing the unstable region reaching all the way to $s=\alpha=0$, allowing a globally stable route from $\alpha=\alpha_{\max}$, $s=0$ to higher s and lower α. Since Eq. (20) shows $d_M\propto\epsilon$, in what follows we use the parameter ϵ alone to label the effects of d_M. This is strictly true for large q: the effect of finite q can be recovered by the substitution $\epsilon\rightarrow\epsilon(1-q^{-2})$. Figure 3(b) shows the effect of the d_M term on the $s-\alpha$ diagram for two values of ϵ. Figure 12 shows the stability boundaries at $\epsilon=0.1$, together with two examples of marginally stable pressure profiles ($\alpha=\alpha(x/L_*)$), one with $r^2/(\mu L_*^2)=25$ and the other having $r^2/(\mu L_*^2)=1/100$. The locations of the discrete mode rational surfaces are shown as points on the two curves, for the choice $n=12$. At high n the mode rational surfaces become closely spaced, requiring that the $\alpha=\alpha(s)$ trajectories are tangential to the stability curve at marginal stability. At lower values of n, $\alpha_{\max}$ may be increased, until one of the mode rational surfaces lies on the marginal $s-\alpha$ boundary. This discreteness of the mode rational surfaces suggests higher $\alpha_{\max}$ values are possible. However, as noted earlier, if $\Delta q=m_0-nq$ is regarded as continuously varying, each mode rational surface may be moved continuously to the next location, ensuring that marginal stability is again determined by the tangent condition. Again we note the importance of $q_{\min}$ passing through integer (or low-order rational) values. This greatly restricts the possible values of Δq and ensures that greater values of $\alpha_{\max}$ are possible.

We have mapped out the stable operating regime in terms of the parameters $\alpha_{\max}$ and $r^2/(\mu L_*^2)$. This is shown

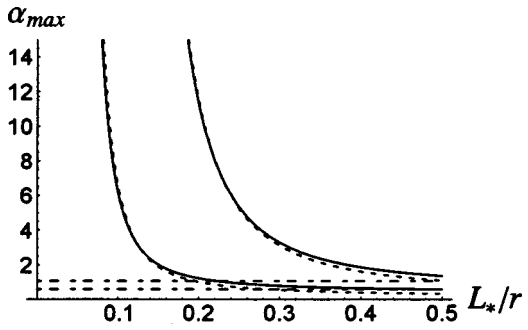

FIG. 13. The infinite-n operating diagram in $\alpha_{\max}-L_*/r$ space for $\epsilon=0.05$ (lower curve) and 0.3 (upper curve) ($\Delta q=0$, $q=3/2$, $\mu=1$). The limits (36) and (37) are shown as dashed lines.

in Fig. 13 for fixed values of n, q, and two representative values of ϵ. Figure 13 demonstrates that there is always stability if α is sufficiently low [$\alpha_{\max}<\alpha_{\rm crit}(\infty)$, the dashed horizontal asymptotes], no matter how large the value of L_*/r, even when $n\to\infty$. One can obtain an analytic scaling for $\alpha_{\rm crit}(\infty)$ from the high-n limit of the eigenvalue condition (19). $\alpha_{\rm crit}(\infty)$ is given by the minimum of α with respect to s on the marginal stability curve, $\gamma=0$. Since for small ϵ we are considering low s, the toroidal coupling term proportional to $\exp(-1/|s|)$ can be ignored. One then finds

$$\alpha_{\rm crit}(\infty)=1.96\epsilon^{1/3}. \tag{36}$$

However there is also stability for $\alpha_{\max}>\alpha_{\rm crit}(\infty)$ if $r^2/(\mu L_*^2)$ is sufficiently large to ensure a trajectory that skirts the nose of the marginal stability boundary. It is also possible to obtain an expression for this limiting value of $\alpha_{\max}$, as a function of L_*/r, in the limit of small L_*/r, i.e., corresponding to a strong ITB. Substituting $x=sr/\mu$, this limiting value, $\alpha_{\rm crit}$, is determined by the intersection of the resulting $\alpha(s)$ given by Eq. (1) with the marginal stability curve including L_*/r. Assuming $sr/L_*\gg 1$ it is possible to solve for $\alpha_{\rm crit}(r/(\mu L_*),\epsilon)$ in this limit:

$$\alpha_{\rm crit}=0.37 s_c^{1/2}\exp[2s_c r/(\mu L_*)], \tag{37}$$

where $s_c>0$ satisfies the transcendental equation

$$0.29\, s_c^{3/2}+1.25\exp(-1/s_c)=\epsilon. \tag{38}$$

For small ϵ, $s_c=2.28\epsilon^{2/3}$ so that $\alpha_{\rm crit}\propto\epsilon^{1/3}$, while for $s_c>0.1$ it is remarkably well fitted by $s_c=0.23+\epsilon$, as shown

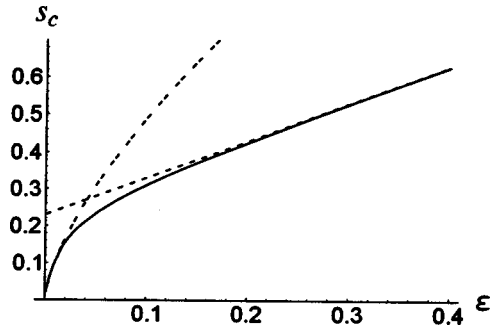

FIG. 14. The critical shear, s_c, as a function of ϵ (solid curve), the asymptotic limit $s_c=2.28\epsilon^{2/3}$ valid as $\epsilon\to 0$ (intermittent dashed line), and the approximate result, $s_c=0.23+\epsilon$, accurate for $\epsilon\gtrsim 0.1$ (dashed line).

in Fig. 14. Equation (36) indicates that the asymptote $\alpha_{\max}=\alpha_{\rm crit}(\infty)$ scales as $\epsilon^{1/3}$ while Eq. (37) shows how large values of $\alpha_{\max}$ are possible for narrow ITBs, i.e., as $\mu L_*/r$ becomes small. This demonstrates that an ITB can sustain high pressure gradients that are stable to ideal MHD ballooning modes, provided the barrier is sufficiently steep. It is also clear from Eqs. (36) and (37) that the increment in α through the ITB ($\Delta\alpha\sim\alpha_{\max}L_*/r$) has a minimum as a function of $r^2/(\mu L_*^2)$, but increases without limit as $r/L_*\to\infty$.

To summarize, there is stability if α is sufficiently low ($\alpha_{\max}<\alpha_{\rm crit}(\infty)$), for any value of L_*/r, but low values of L_*/r permit arbitrarily steep barriers, as indicate by Eq. (37). Although we have derived the above results using the lowest order ballooning theory, the very existence of a consistent description of the radial mode structure at low s depends on there being a solution of the recurrence relation.

VIII. EFFECT OF THE BOOTSTRAP CURRENT

The steep plasma gradients associated with an ITB drive a large bootstrap current, $j_{\rm bs}$,[27] which can modify the magnetic shear. In a large aspect ratio tokamak, $j_{\rm bs}$ takes the form[28]

$$j_{\rm bs}=-\frac{\epsilon^{-1/2}q}{B_0}\left[2.44(T_e+T_i)\frac{dn_e}{dr}+0.69n_e\frac{dT_e}{dr}-0.42n_e\frac{dT_i}{dr}\right], \tag{39}$$

where n_e is the electron density and $T_{e,i}$ are the electron and ion temperatures. This can be expressed as

$$j_{\rm bs}=\frac{\alpha B_0}{qR}f(\tau,\eta_e,\eta_i), \tag{40}$$

where

$$f(\tau,\eta_e,\eta_i)=\frac{2.44(1+\tau)+0.69\eta_e\tau-0.42\eta_i}{2(1+\tau+\eta_e\tau+\eta_i)} \tag{41}$$

with $\tau=T_e/T_i$ and $\eta_j=d(\ln T_j)/d(\ln n_e)$. As a result the magnetic shear, s, can be written as

$$s=s_\infty-(\alpha/\epsilon^{1/2})f(\tau,\eta_e,\eta_i), \tag{42}$$

where s_∞ is the background shear in the absence of the ITB. Thus large values of α can lead to negative values of s, even if $s_\infty>0$. The effect of $j_{\rm bs}$ is largest for electron density barriers: taking $\tau=1$ for simplicity, $f\to 0.07$ if $\eta_e=\eta_i\gg 1$, whereas $f\to 0.61$ for $\eta_{e,i}\cong 0$.

One could deduce the trajectory in $s-\alpha$ corresponding to a general $s_\infty(x)$ and $\alpha(x)$ and determine the conditions for stability to high-n modes. However, since $j_{\rm bs}$ can lead to $s<0$, even for constant s_∞, we consider just this case to illustrate its impact. Clearly Eq. (42) then follows a linear trajectory whose gradient depends on $f(\tau,\eta_e,\eta_i)$ and ϵ, provided $d_M>0$, this can remain in a stable region of $s-\alpha$ if s_∞ is not too large, as shown in Fig. 15. Here the profile trajectory starts from s_∞ and α_∞ (the value of α remote from the ITB) at its left-hand end, traverses to $s(\alpha_{\max})$ and $\alpha_{\max}$ at its right-hand end, i.e., the center of the ITB, and then returns to s_∞ and α_∞ as it emerges from the ITB on the other side. Clearly

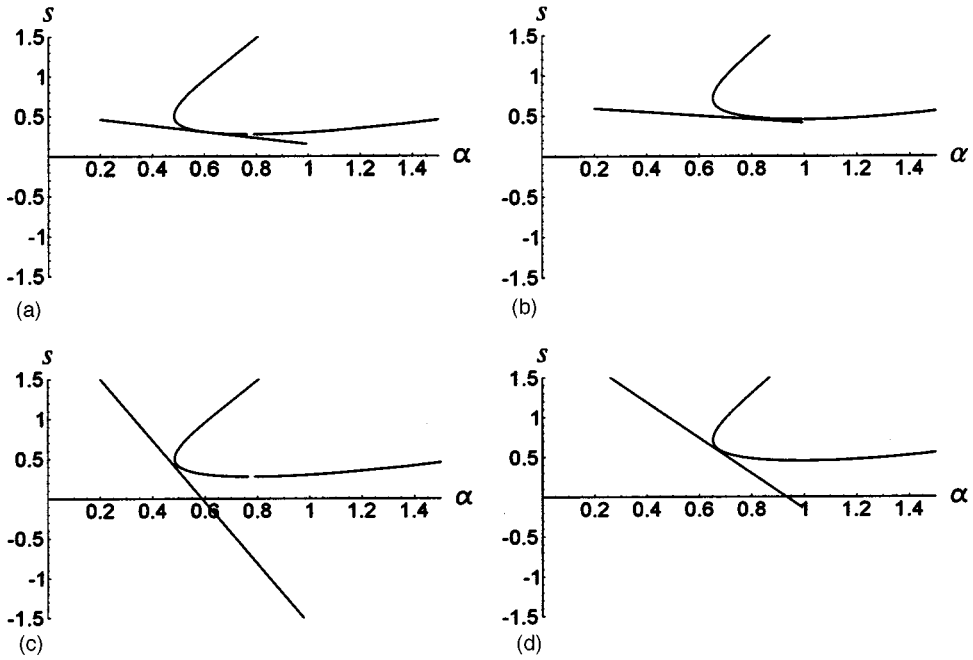

FIG. 15. The effect of the bootstrap current on stability, showing the profile trajectory and infinite-n stability boundaries for different parameters: (a) $\epsilon=0.1$, $\eta_{e,i}=20$, leading to $s_{\infty c}=0.46$; (b) $\epsilon=0.3$, $\eta_{e,i}=20$, leading to $s_{\infty c}=0.59$; (c) $\epsilon=0.1$, $\eta_{e,i}=0$, leading to $s_{\infty c}=1.50$; (d) $\epsilon=0.3$, $\eta_{e,i}=0$, leading to $s_{\infty c}=1.63$ ($\alpha_\infty=0.2$, $\alpha_{\max}=1.0$, $q=2$, $\tau=1$ in all cases).

this imposes no limit on $\alpha_{\max}$: increasing $\alpha_{\max}$ merely takes the trajectory into the stable $s<0$ region. Again one can calculate the limiting stable trajectory, namely when Eq. (42) is tangential to the $s-\alpha$ stability boundary, $\alpha(s)$.

Comparing Figs. 15(a), 15(b) with Figs. 15(c), 15(d) we see that varying ϵ (at fixes q) has only a weak effect on the critical value, $s_{\infty c}$, of s_∞. For example, when $\eta_{e,i}=20$, $s_{\infty c}$ varies from 0.46 to 0.59 as ϵ varies from 0.1 to 0.3. This can be understood as follows: as discussed in Sec. VII, the stability boundary migrates towards $s=\alpha=0$ as $d_M^{1/3}\propto\epsilon^{1/3}$, whereas the slope of the trajectory increases as $\epsilon^{-1/2}$, so that the net effect is very weak, proportional to $\epsilon^{-1/6}$. However, there is a stronger effect if $q\to 1$, since this implies $d_M\to 0$ without having an effect on the profile trajectory (42). The value of $s_{\infty c}$ has a much stronger dependence on $\eta_{e,i}$, as shown by comparing either of the pairs Figs. 15(a) and 15(b) or Figs. 15(c) and 15(d). Taking the case $\epsilon=0.1$ as an example, $s_{\infty c}\cong 0.46$ for $\eta_{e,j}=20$, whereas $s_{\infty c}=1.50$ for $\eta_{e,i}=0$.

Thus consideration of a self-consistent treatment of the bootstrap current together with favorable average curvature, shows that there is no limit on $\alpha_{\max}$, provided the background magnetic shear exceeds a critical value; this critical value is larger for density barriers than thermal ones.

IX. FLOW SHEAR EFFECTS

Internal transport barriers are associated with a region of strongly sheared toroidal plasma flow. Such flows tend to stabilize ideal MHD ballooning modes.[29,30] Their main effect in the stability analysis is to introduce a radially varying Doppler shift to the mode frequency:

$$\gamma\to\gamma+in\Omega(x), \tag{43}$$

where Ω is the toroidal angular velocity of the flow, normalized to the Alfvén frequency, into the dispersion relation (19). This in turn modifies the coefficient of c_m in the recurrence relation (27). Because of the explicit n in the replacement (42), this dependence will often dominate profile effects from $\alpha(x)$, e.g., if flows exceed diamagnetic levels.

In the simple case of both constant magnetic shear and flow shear,[29,30] an analysis similar to that in Appendix C leads to a set of modes with the structures (C7) [i.e., with Fourier amplitudes $J_m(\lambda/\kappa_\Omega)\equiv I_m(\lambda/|\kappa_\Omega|)$, where $\kappa_\Omega=-id\Omega/dq\sim O(1)$ and I_m is a modified Bessel function[23]], each centered on a different mode resonant surface, say $m=p$, and having a corresponding real frequency $\Omega=\Omega_0+pd\Omega/dq$. Since these frequencies differ by $O(1)$ the modes do not couple significantly, so that each corresponds to an eigenmode. The value of p corresponding to the maximum value of γ_0 will give the most unstable mode. Because $\lambda\propto\exp(-1/|s|)$ the harmonic content of these "extended" modes is in fact limited to $m=p$ for finite $(d\Omega/dq)$.

In the presence of an ITB the plasma flow is normally localized near the barrier and a more realistic model for the toroidal angular velocity of the flow is given by a similar form to Eq. (1) for $\alpha(x)$, namely:

$$\Omega=\Omega_0\,\mathrm{sech}^2(x/L_\Omega). \tag{44}$$

The flow shear can then have a similar effect to the α profile in destroying extended ballooning structures. For simplicity we consider constant but low values of s, retain terms quadratic in x from Eq. (44) and neglect the variation in $\alpha(x)$. Replacing $\hat{\gamma}^2$ in the recurrence relation by the correct inertial form γs but with the substitution (43) we see that we replace

κ in Eq. (28) by $\kappa_\Omega = -i(\Omega_0/2)(r/nqsL_\Omega)^2$. Therefore we expect to obtain a transition to a narrow spectrum of modes when $|\nu_\Omega| \sim 1$, where $\nu_\Omega = \lambda/\kappa_\Omega$, i.e.,

$$r/(qsL_\Omega) \sim n(5\alpha/4\Omega_0)^{1/2} \exp(-1/2|s|). \tag{45}$$

Solutions of the recurrence relation could be solved with the form (2) for q near $q_{\min}$, but basically one would find a mode with a real frequency Ω_0 whose growth rate is given by $\gamma s = \gamma_0^2$.

X. DISCUSSION AND CONCLUSIONS

We have explored the stability of configurations with low magnetic shear, s, including those with a minimum in q, which are of interest to tokamak discharges with ITBs. Before discussing our results in detail we list the principle outcomes of this work.

(1) At low s, a novel recurrence relation approach has been developed; this replaces and complements the ballooning transformation, which fails in precisely this regime for reasonable values of n.
(2) This has been used to analyze the stability of the $s-\alpha$ equilibrium at low s: considerations of the global stability of an entire α profile imply that the concept of second stability is of limited significance.
(3) However the recurrence approach incorporates effects from the discreteness of mode rational surfaces, entirely absent from the ballooning transformation, even at high-n.
(4) This does allow the possibility of bands of stability in the second stable region, but for constant shear these are not of practical significance, other than interpreting results from more sophisticated MHD codes.
(5) However, analysis of the situation with a minimum in q demonstrates that low order rational values of $q_{\min}$ are particularly stable as a consequence of these discreteness effects.
(6) Inclusion of the stabilizing effects of favorable average curvature in the case of $q_{\min}$ allows high stable values of α when the ITB is sufficiently narrow.
(7) Consideration of the bootstrap contribution to the magnetic shear in the presence of favorable curvature shows that stable ITB configurations with finite shear are possible; the required shear is lower for density barriers than for thermal ones.
(8) Plasma flow shear can readily break up ballooning mode structures, particularly at low s.

Now we discuss these points in more detail. The fact that $s \propto x$ near $q_{\min}$, where x is the distance from $q_{\min}$ as shown in Eq. (12), has necessitated exploration of the validity of the ballooning representation at low s. At small s the stability of ballooning modes can be studied using a two-scale analysis of the lowest order ballooning equation. A straightforward application of this approach fails to provide an equation for the radial envelope of a ballooning mode. One can recover the exponentially small terms that determine this by invoking a variational approach with the two-scale solution as a trial function; this provides an analytic expression, Eq. (19), for the WKB wave-number $k(x,\gamma)$ of the ballooning modes as a function of the radial profiles of s and α. [In the case of equilibria with a $q_{\min}$ surface, a minor modification of the eikonal in the ballooning transformation is necessary, Eq. (10), but this merely leads to an eigenvalue equation that recognizes the x dependence of s.]

It transpires from a WKB analysis that stringent conditions on the largeness of n must be imposed (see Fig. 5) if the ballooning representation is to be valid for modes located at low s. These values of n ($nq > \exp(1/|s|)$) can be well beyond those needed for the applicability of a simple MHD plasma model [for example, the condition that the wavelength is greater than the ion Larmor radius, ρ, i.e., $n < (a/\rho q)$, could be typically $n < 10^2$; diamagnetic effects could enter at even lower values]. Furthermore, as s decreases the ballooning representation predicts a transition from modes localized near the maximum value of α to a type of mode located on a linear part of the α profile which, at $s \sim 1$, would be more extended. However, at small s these are in fact narrower modes than those located at the maximum α and therefore less important.

At lower values of n the extended ballooning mode collapses onto isolated modelets at each rational surface (Fig. 2). The effect of finite-n and profile effects on these structures can be analyzed using the three-term recurrence relation, Eq. (27) satisfied by the amplitudes of these modelets. The validity of this three-term recurrence relation depends precisely on small s, so this technique provides just the required complementary approach to the ballooning representation that itself fails in this very situation. [Indeed for more complex geometries the localized modelets may contain a rich harmonic content, but the recurrence relation will continue to involve only c_m and $c_{m\pm1}$-space couplings to $c_{m\pm p}$ will be $\sim \exp(-p/|s|)$, hence exponentially smaller for small s.] This approach allows us to follow the transition from extended ballooning mode structures to a narrow spectrum of modelets as magnetic shear reduces and finite-n effects increase. For the simple cases of constant s and an α profile with a maximum and one that is linear, analytic solutions can be obtained; in more general cases, such as the profiles associated with an ITB, numerical solutions are readily obtained. For the case of constant s and an α profile given by Eq. (1), Fig. 5 compares stability boundaries resulting from the recurrence relation with those from the ballooning representation, while Fig. 9 shows how mode structures narrow as s decreases.

It is worth emphasizing that when the stability of a whole profile is considered second stability can become meaningless at high n: even if $\alpha_{\max}$ lies in "second stability" [$\alpha_{\max} > \alpha_2(s)$], unstable lower values of α are inevitable somewhere in the profile. However consideration of moderate n effects, say $n \sim 15$, shows that stable bands can exist even for $\alpha > \alpha_2(s)$ as shown in Fig. 6. Figure 8 shows the effect on the bands of different values of $\Delta q = m_0 - nq$. Both these figures show how the predictions from the recurrence relation for the stable bands can be well represented by analytic results obtained from the positions in the $s-\alpha$ stability diagram of the mode rational surfaces near $q_{\min}$. Thus, if for example, the mode rational surface nearest to $\alpha_{\max}$ lies be-

yond α_2, yet the adjacent ones lie below α_1, then the configuration should be stable as no harmonic lies in the unstable zone. However, it is unlikely that one can control Δq during the evolution of q and $\alpha_{\max}$ in a tokamak, particularly for higher n, so these bands will have little practical significance. Nevertheless, these results may be of value for interpreting the output of MHD stability codes used to analyze ITBs.

Turning to the situation of interest, profiles corresponding to an ITB at a discharge with a minimum in q, the recurrence relation has been solved using representative α and s profiles given by Eqs. (1) and (12), respectively. At constant n and q, this situation is parameterized by two key quantities: $\alpha_{\max}$ and $r^2/(\mu L_*^2)$. These govern the trajectory of the equilibrium profiles in the $s-\alpha$ stability diagram. For large $\alpha_{\max}$ and $r^2/(\mu L_*^2)$ the trajectory crosses the unstable region at higher s values: the location being dominated by the α profile. For such a situation an unstable mode is found, located away from $q_{\min}$ and more extended in m; nevertheless the exponentially weak toroidal coupling at low s results in a somewhat asymmetric m-spectrum. For lower $r^2/(\mu L_*^2)$ the trajectory crosses the unstable region at lower s and the presence of $q_{\min}$ dominates the behavior: the spectrum is located near $s=0$ and is somewhat narrower and asymmetric, as shown in Fig. 11. (Of course, moving inwards into regions of negative s, one only encounters stable regions in the $s-\alpha$ model.) In all cases the extremely weak coupling at low s prevents ballooning mode structures penetrating to $q_{\min}$. Again it is possible to locate bands of stability due to moderate n when $\alpha_{\max}$ lies beyond α_2. Unlike the case of constant shear, the existence of this effect indicates that discharges with low order rational values of $q_{\min}$ will have particularly favorable stability properties. It is interesting that, experimentally, ITB formation appears to be facilitated in these circumstances.

The simple $s-\alpha$ model clearly does not allow globally stable ITB equilibrium profiles at high n. However inclusion of the formally small, in inverse aspect ratio ϵ, terms associated with favorable average curvature, Eq. (21), has a dramatic effect on the low s part of the stability boundary, as shown in Fig. 3(b). In fact it allows a stable route from high $\alpha_{\max}$ and low s, characteristic of the ITB pedestal profile, to low α and moderate s as appropriate to magnetic surfaces away from the ITB itself. The solution of the recurrence relation then allows us to construct an operating diagram (Fig. 13), parametrized in terms of $\alpha_{\max}$, ϵ, and $r^2/(\mu L_*^2)$ (for given n and q), for ITB discharges that are globally stable to high-n ideal MHD modes. This diagram shows that ITBs with high $\alpha_{\max}$ can be stable if $r^2/(\mu L_*^2)$ is sufficiently high, i.e., the barrier is narrow. Equations (36) and (37) provide analytic scalings for the limiting values of $\alpha_{\max}$ with ϵ, namely $\epsilon^{1/3}$ for small ϵ, in the two limits of small and large L_*/r.

One can, of course, reach similar conclusions based on the lowest order $s-\alpha$ stability diagram. However a key point is that at low s no consistent higher order theory exists within the ballooning representation: one is certainly not describing radially extended ballooning modes at low s. The recurrence relation technique provides a sound approach, which precisely complements the failing ballooning theory at low s. Although stability boundaries remain approximately the same, the modes only couple a small number of rational surfaces.

The self-consistent treatment of the effect of the bootstrap current on the required magnetic shear near an ITB shows that, in the presence of favorable curvature, one can have stable profiles at finite background shear. There is then no limit on the maximum pressure gradient in the ITB, provided that the background shear, s_∞, is less than a critical value, $s_{\infty c}$. The values of $s_{\infty c}$ typically lie above 0.5, with thermal barriers requiring lower values than density barriers, as shown in Fig. 15.

Finally, we have briefly investigated the impact of a sheared plasma rotation, Ω, with the profile given in Eq. (44), on the mode frequency and growth, estimating when this disrupts extended ballooning modes in Eq. (45).

In summary, we have explored the stability of ideal MHD ballooning modes at moderate to high n for a situation corresponding to an internal transport barrier near a minimum in q. This configuration has been modelled by the $s-\alpha$ equilibrium, self-consistently taking account of the low shear near $q_{\min}$, Eq. (12), and the steep pressure gradients in the barrier in the radial profiles of $\alpha(x)$, Eq. (1). The stability of such profiles depends on following their trajectory in the $s-\alpha$ stability diagram, suitably modified for finite-n profile effects. The effects of including the stabilizing finite-n and favorable average curvature at low s have been shown to be important for the overall stability of an ITB configuration. Low order rational values of $q_{\min}$ have been shown to have particularly favorable stability properties. Furthermore, the combination of favorable average curvature and the bootstrap current is shown to allow unlimited values of $\alpha_{\max}$ for finite values of magnetic shear. The effects of plasma flow shear have also been briefly addressed.

ACKNOWLEDGMENTS

This work was funded jointly by the United Kingdom Engineering and Physical Sciences Research Council and by EURATOM.

APPENDIX A: THE INERTIAL TERM

The eigenvalue $\hat{\gamma}^2$ introduced in Eq. (3) is a fictitious growth rate, it really only measures instability. A correct form of the inertia operator that includes contributions from toroidal and poloidal displacements is

$$\gamma^2\left[1+\left(\frac{ir}{nq}\frac{\partial}{\partial x}+\alpha\sin\theta\right)^2\right]. \tag{A1}$$

If this is followed through to the variational expression in ballooning space, Eq. (18), we modify the inertial term:

$$\hat{\gamma}^2 \rightarrow \gamma^2 G. \tag{A2}$$

However with the trial function V from Eq. (16) the integral over η no longer converges for the inertial term. With this correct inertia the trial function should reflect the appropriate asymptotic behavior at large η:

$$V \propto \exp(-\gamma|\eta|). \tag{A3}$$

We therefore replace the trial function $V_0(u)=1$, by the analytic form

$$V_0(u)=\mathrm{sech}(\gamma s u). \tag{A4}$$

Provided $\gamma s \ll 1$, the integrals over the other terms in Eq. (18) are essentially unchanged. Thus the harmonic terms can still be evaluated by contour integration, but the new poles arising from the form (A4) occur at $u=(2n+1)\pi i/(\gamma s)$. These are more remote than those retained at $u=\pm i$ when $\gamma s \ll 1$, which is assumed since we are interested in near marginal stability. The other, nonharmonic, terms merely acquire corrections of $O(\gamma s)$. The inertial term now converges to give a contribution γs in Eq. (19), where γ now does represent the linear growth rate.

APPENDIX B: A MORE EXACT VARIATIONAL $s-\alpha$ DISPERSION RELATION

The dispersion relation of Sec. III was derived using the ballooning transformation and a variational expression of the form,

$$H(\alpha,s,k)=\sum_{n=0}^{4}\alpha^{2n}H_n(s) - \sum_{n=1}^{8} I_n(\alpha,s)\exp(-n/|s|)\cos(nk), \tag{B1}$$

where the integrals in Eq. (18) were evaluated by expanding $G^{-1}(\alpha,s)$ up to $O(\alpha^3)$ in order to generate an expression which predicts first and second stability boundaries at low shear. Because marginal stability at low shear requires the ordering $\alpha^2/s \approx O(1)$ the terms H_0, H_1, and H_2 are all required in Eq. (B1). For $s \ll 1$, the dominant appearance of $\cos(nk)$ in $H(s,\alpha,k)$ is clearly determined by $I_1(\alpha,s)$, and so we retained only these terms (H_0, H_1, H_2, and I_1) in the variational treatment, and for use in deriving the recursion equation. In particular the neglect of all higher order coupling terms (I_n, for $n \geqslant 2$) generates a tridiagonal matrix in the recursion problem, permitting analytic solution in some cases (Sec. IV) and rapid numerical solution in general. However, an exact evaluation of the coupling coefficient $I_1(\alpha,s)$ leads to a rather cumbersome expression so, following Pogutse and Yurchenko,[11] we approximated I_1 by its lowest power in α, and neglected contributions of order $s^{\ell}(\ell=1-3)$ relative to 1 within this term. Thus we obtained $I_1(\alpha,s) \simeq 5\alpha/4$.

In this appendix we demonstrate that, at the values of s of interest, this is a satisfactory approximation for I_1. In order to avoid the need to sum the infinite series in α arising from the expansion of G^{-1}, we revert to a different variational object, derived directly from the $s-\alpha$ equation (7) without introducing the transformation of Ref. 11, $\zeta \rightarrow V/\sqrt{G}$; i.e., we use

$$\hat{H}(\alpha,s,k)=\int_{-\infty}^{\infty} d\eta \left\{ [1+(t-\alpha\sin\eta)^2]\left(\frac{\partial\zeta}{\partial\eta}\right)^2 - \alpha\zeta^2[\cos\eta+\sin\eta(t-\alpha\sin\eta)]\right\}, \tag{B2}$$

with $t \equiv s(\eta-k)$, and we employ the trial function

$$\zeta=\zeta_0+\zeta_1+\zeta_2+\zeta_3, \tag{B3}$$

where

$$\begin{aligned}
\zeta_0&=1/\sqrt{1+t^2},\\
\zeta_1&=\frac{\alpha\zeta_0}{(1+t^2)}[\cos\eta+t\sin\eta],\\
\zeta_2&=\frac{3}{4}\frac{\alpha^2\zeta_0}{(1+t^2)^2}[\cos 2\eta+t\sin 2\eta]-\frac{1}{2}\frac{\alpha^2\zeta_0}{(1+t^2)}\cos 2\eta,\\
\zeta_3&=\frac{\alpha^3\zeta_0}{(1+t^2)^3}\left\{\frac{7}{12}[\cos 3\eta+t\sin 3\eta] - \frac{3}{2}[\cos\eta+t\sin\eta]\right\}\\
&\quad+\frac{\alpha^3\zeta_0}{(1+t^2)^2}\left\{\frac{5}{8}\cos\eta+\frac{1}{4}t\sin\eta-\frac{11}{24}\cos 3\eta - \frac{1}{4}t\sin 3\eta\right\}+\frac{2\alpha s\zeta_0}{(1+t^2)^2}\{\cos\eta+2t\sin\eta\}.
\end{aligned} \tag{B4}$$

This choice of trial function makes use of the systematic expansion of the $s-\alpha$ equation for low magnetic shear, with $\alpha^2/s=0(1)$. Inserting this expression for ζ into Eq. (B2) and evaluating all the integrals $\int_{-\infty}^{\infty} d\eta$ analytically, generates a finite series of terms in α^n containing harmonic terms proportional to $\cos(nk)$ for $n=0$, up to $n=8$, so that it is clear that the form (B1) must result. The $n=0$ terms, i.e., those independent of k, are conveniently gathered using an ordering in which $\alpha^2/s=0(1)$. This yields the result,

$$\hat{H}=\frac{1}{2}s^2-\frac{3}{4}\alpha^2 s+\frac{18}{128}\alpha^4+0(\alpha^6) - \sum_{n=1}^{\infty} I_n e^{-n/|s|}\cos nk. \tag{B5}$$

For comparison, using the choice of trial function from Ref. 11 in H yields an expression that, apart from the $\cos nk$ coupling terms, only differs in the α^4 contribution (having the coefficient 19/128). However Eq. (B5) predicts the low magnetic shear stability boundaries with slightly greater accuracy.

As noted above, an exact evaluation of all terms in Eq. (B2) contributing to $I_1(\alpha,s)$ is lengthy and leads to a somewhat unwieldy expression. However, its exact form has been calculated and takes the form:

$$I_1(\alpha,s)=-\alpha\sum_{n=0}^{3}\sum_{m=0}^{n+5}\left(\frac{\alpha^2}{s^2}\right)^n s^m c_{nm}, \tag{B6}$$

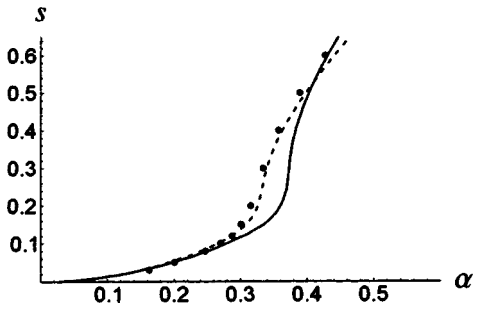

FIG. 16. Comparison of stability boundaries using: (i) $\hat{H}(\alpha,s,k=0)$ with the exact $I_1(\alpha,s)$ (dashed curve) and (ii) $H(\alpha,s,k=0)$ with $I_1=1.25\alpha$ (solid curve), with (iii) the numerical solution of the $s-\alpha$ equation (7) (dots).

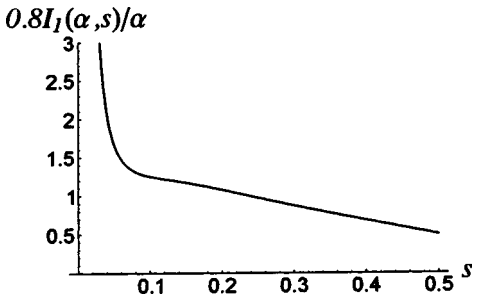

FIG. 17. Comparison of the approximation $I_1=1.25\alpha$ with the exact $I(\alpha,s)$, Eq. (B6), evaluated along the first stability boundary, $\alpha=\alpha_1(s)$, showing reasonable agreement over the range of relevant α values.

where the c_{nm} are rational numbers with

$$
\begin{aligned}
c_{0m}&=\{-4;5;10;5;0;0\}\div 4,\\
c_{1m}&=\{104;-1334;-4618;-6408;-3945;+2040;\\
&\quad -420\}\div 1536,\\
c_{2m}&=\{-12\,077;-134\,197;756\,981;1\,429\,740;\\
&\quad 4\,958\,175;10\,891\,665;6\,965\,550;280\,350\}\\
&\quad \div 4\,423\,680,\\
c_{3m}&=\{-1134;-103\,946;-833\,126;-3\,054\,465;\\
&\quad -5\,401\,935;-4\,701\,810;-10\,599\,930;\\
&\quad -28\,206\,045;-3\,241\,350\}\div 53\,084\,160,
\end{aligned}
\tag{B7}
$$

where we explicitly exhibit the rationality.

An extremely accurate dispersion relation, predicting stability boundaries which agree closely with those obtained by numerical solution of the full $s-\alpha$ equation, is obtained by using this evaluation of $I_1(\alpha,s)$ together with all terms in the k-independent part of $\hat{H}$, up to and including $0(\alpha^8)$ [within an $s\sim 0(\alpha^2)$ ordering scheme]; i.e.,

$$
\begin{aligned}
\hat{H}(\alpha,s,k)&=\frac{1}{2}s^2\left[1-\frac{3}{4}\sigma+\frac{18}{128}\sigma^2\right]\\
&\quad +s^2\alpha^2\left[-\frac{3}{4}+\frac{25}{64}\sigma-\frac{5}{64}\sigma^2\right]\\
&\quad +\alpha^2 s^3[-63360+91278\sigma-44622\sigma^2\\
&\quad +9113\sigma^3]/73728-I_1(\alpha,s)\exp(-1/|s|)\cos k,
\end{aligned}
\tag{B8}
$$

with $\sigma=\alpha^2/s$. The marginal stability boundary predicted by Eq. (B8) is shown in Fig. 16 (dashed curve), along with exact results from solution of the $s-\alpha$ equation (7) (dots) and the approximation for H, Eq. (19), used in the text (solid curve).

The result of evaluating $I_1(\alpha,s)/1.25\alpha$ along the stability boundary in Fig. 16 is shown in Fig. 17. This demonstrates that the approximation $I_1\simeq 1.25\alpha$, used in the recursion calculations, is fairly accurate throughout the range of s where harmonic coupling is significant. At very small s, where $I_1\neq 1.25\alpha$, this coupling is negligible.

APPENDIX C: RECURRENCE RELATION SOLUTION WITH A LINEAR PROFILE

In this appendix we derive the solution of the recurrence relation with a linear profile of the growth rate γ_0^2, namely Eq. (33) reproduced below

$$(\hat{\gamma}^2-\gamma_0^2-\kappa_1 m)c_m-\lambda(c_{m+1}+c_{m-1})=0. \tag{C1}$$

This can be recognized as the recursion relation that follows from the Fourier series solution to the differential equation

$$i\kappa_1\frac{du}{d\tau}+[(\hat{\gamma}^2-\gamma_0^2)-2\lambda\cos\tau]u=0. \tag{C2}$$

This has the solution

$$u(\tau)=\exp\left(\frac{i}{\kappa_1}\int^{\tau}d\tau[\hat{\gamma}^2-\gamma_0^2-2\lambda\cos\tau]\right) \tag{C3}$$

which must be periodic on 2π, providing the eigenvalue condition

$$\oint d\tau[\hat{\gamma}^2-\gamma_0^2]=2\pi p\kappa_1 \tag{C4}$$

for any integer p, i.e.,

$$\hat{\gamma}^2=\gamma_0^2+p\kappa_1 \tag{C5}$$

corresponding to Eq. (34). The lowest order $(p=0)$ eigenfunction follows from the Bessel function expansion[23] of Eq. (C3):

$$
\begin{aligned}
u(\tau)&=\exp\left[ip\tau-i\left(2\frac{\lambda}{\kappa_1}\right)\sin\tau\right]\\
&=\sum_{m=-\infty}^{\infty}\exp(-im\tau)J_{m-p}\left(\frac{2\lambda}{\kappa_1}\right)
\end{aligned}
\tag{C6}
$$

so that

$$c_m = J_{m-p}\left(\frac{2\lambda}{\kappa_1}\right). \tag{C7}$$

The asymptotic behavior of J_{m-p} in the WKB limit, $2\lambda/\kappa_1 \gg 1$, shows that the c_m decay exponentially for $|m| > 2\lambda/\kappa_1 \gg 1$ and that adjacent c_m have the same sign for large positive m, while they alternate for large negative m.[24]

[1] F. M. Levinton, M. C. Zarnstorff, S. H. Batha *et al.*, Phys. Rev. Lett. **75**, 4417 (1995).

[2] Y. Koide, M. Kikuchi, M. Mori *et al.*, Phys. Rev. Lett. **72**, 3662 (1994); T. Fujita, S. Ide, H. Shirai, M. Kikuchi, O. Naito, Y. Koide, S. Takeji, H. Kubo, and S. Ishida, *ibid.* **78**, 2377 (1997).

[3] E. J. Strait, L. L. Lao, M. E. Mauel *et al.*, Phys. Rev. Lett. **75**, 4421 (1995).

[4] JET Team and C. Gormezano, in *Proceedings of the 16th International Conference on Fusion Energy*, Montreal, 1996 (IAEA, Vienna, 1997), Vol. 1, p. 487; J. Paméla and contributors to EFDA-JET programme, in *Proceedings of the 18th International Conference on Fusion Energy*, Sorrento, 2000 (IAEA, Vienna, 2001), CD-ROM, post deadline paper PD/1.

[5] J. W. Connor, T. Fukuda, X. Garbet, C. Gormezano, V. Mukhovatov, M. Wakatani, the ITB Database Group, and the ITPA Topical Group on Transport and Internal Barrier Physics, ''A review of internal transport barrier physics for steady state operation of tokamaks,'' Nucl. Fusion (to be published).

[6] R. C. Wolf, Plasma Phys. Controlled Fusion **45**, R1 (2003).

[7] J. W. Connor, R. J. Hastie, and J. B. Taylor, Phys. Rev. Lett. **40**, 396 (1978).

[8] J. W. Connor and J. B. Taylor, Phys. Fluids **30**, 3180 (1987).

[9] F. Romanelli and F. Zonca, Phys. Fluids B **5**, 4081 (1993).

[10] J. W. Connor and R. J. Hastie, in *Proceedings of the 30th European Conference on Controlled Fusion and Plasma Physics*, St. Petersburg, 2003 (European Physical Society, Mulhouse, 2003), ECA Vol. 27A, paper P 3.94 (http://eps2003.ioffe.ru/public).

[11] O. P. Pogutse and E. I. Yurchenko, in *Reviews of Plasma Physics*, edited by M. A. Leontovich (Consultants Bureau, New York, 1986), Vol. 11, p. 65; JETP Lett. **6**, 318 (1968) [Pis'ma Zh. Eksp. Teor. Fiz. **28**, 344 (1978)].

[12] C. Mercier, in *Proceedings of the 7th International Conference on Plasma Physics and Controlled Nuclear Fusion Research*, Innsbruck, 1978 (IAEA, Vienna, 1979), Vol. 1, p. 701.

[13] J. W. Connor and R. J. Hastie, Phys. Rev. Lett. (to be published).

[14] J. W. Connor, R. J. Hastie, and J. B. Taylor, Proc. R. Soc. London, Ser. A **365**, 1 (1979).

[15] R. L. Dewar and A. H. Glasser, Phys. Fluids **26**, 3038 (1983).

[16] J. W. Connor, J. B. Taylor, and H. R. Wilson, Phys. Rev. Lett. **70**, 1803 (1993).

[17] J. B. Taylor, J. W. Connor, and H. R. Wilson, Plasma Phys. Controlled Fusion **35**, 1063 (1993).

[18] D. Lortz and J. Nührenberg, Phys. Lett. **68A**, 49 (1978).

[19] H. R. Strauss, Phys. Fluids **24**, 2004 (1981).

[20] O. P. Pogutse, N. V. Chudin, and E. I. Yurchenko, Sov. J. Plasma Phys. **9**, 96 (1983).

[21] D. Lortz and J. Nührenberg, Nucl. Fusion **19**, 1207 (1979).

[22] B. Coppi, A. Ferreira, and J. J. Ramos, Phys. Rev. Lett. **44**, 990 (1980).

[23] M. Abramowitz and I. A. Stegun, *Handbook of Mathematical Functions* (Dover, New York, 1965).

[24] J. B. Taylor and H. R. Wilson, Plasma Phys. Controlled Fusion **38**, 1999 (1996).

[25] R. J. Hastie and J. B. Taylor, Nucl. Fusion **21**, 187 (1981).

[26] Y. Kishimoto, J.-Y. Kim, T. Fukuda, S. Ishida, T. Fujita, T. Tajima, W. Horton, G. Furnish, and M. J. Lebrun, in *Proceedings of the 16th International Conference on Fusion Energy*, Montreal, 1996 (IAEA, Vienna, 1997), Vol. 2, p. 581; J.-Y. Kim, Y. Kishimoto, M. Wakatani, and T. Tajima, Phys. Plasmas **3**, 3689 (1996).

[27] R. J. Bickerton, J. W. Connor, and J. B. Taylor, Nature (London), Phys. Sci. **229**, 110 (1971).

[28] R. D. Hazeltine, F. L. Hinton, and M. N. Rosenbluth, Phys. Fluids **16**, 1645 (1973).

[29] R. L. Miller, F. L. Waelbroeck, A. B. Hassam, and R. E. Waltz, Phys. Plasmas **2**, 3676 (1995).

[30] A. J. Webster and H. R. Wilson, in *Proceedings of the 30th European Conference on Controlled Fusion and Plasma Physics*, St. Petersburg, 2003 (European Physical Society, Mulhouse, 2003), ECA Vol. 27A, paper 0-4.1A (http://eps2003.ioffe.ru/public).